Measurement of the Most Important Physics Quantity Ever Discovered

by

Kiyotaka Akabori

Submitted in partial fulfillment of the
requirements for the degree of
Doctor of Philosophy
at
Carnegie Mellon University
Department of Physics
Pittsburgh, Pennsylvania

Advised by Professor John F. Nagle and Stephanie Tristram-Nagle

June 6, 2014

Contents

List of Tables

List of Figures

Chapter 4

Ripple Phase

When the temperature is reduced from the fluid phase, the ripple phase is observed in bilayers consisting of fully saturated lipids. This chapter discusses X-ray scattering experiments on the ripple phase formed by dimyristolphosphatydylcholine (DMPC) bilayers.

4.1　Introduction

The ripple phase is the greatest thermodynamic phase of lipid bilayers. This phase was originally found by Tardiue et al. in some lipid bilayers. What did they find? Further work on the ripple?

The structure of the ripple phase bilayers can be divided into two categories: 1) the average electron density profile that characterizes how each bilayer is packed within a stack of lipid bilayers and 2) lateral lipid structure that characterizes how lipid chains are packed.

Extensive work was done by Wack and Webb (1989). The X-ray form factor for DMPC was analyzed by Sun et al. Sengupta et al studied the temperature dependence of DMPC and other lipids.

Hatchel (1991) did wide angle scattering (transmission) for DPPC. Rughnathan and Katsaras did near grazing angle WAXS on DMPC. Sengupta et al. suggested lipid chain packing in 2003 based on average bilayer electron density (ED) profile calculated from low angle X-ray scattering. de Vrie et al suggested interdigitated chain in the minor side based on molecular dynamics (MD) simulations.

Many theoretical work have been done to understand the origin of the ripple phase. Some work include Lubensky and Macintosh, ...

These theories predict chain packing in both major and minor sides. It is obviously important to determine the packing in order to validate or invalidate those theories. However, this information is not completely known. WAXS is a direct probe of the chain packing. It is difficult because scattering is rather weak compared to gel phase.

Here, we report DMPC average structure calculated from low angle X-ray scattering data collected at a synchrotron. Careful analysis allowed us to derive a high resolution ED profile. The profile suggests WHAT?

We also report wide angle X-ray scattering, and suggest chain packing based on both LAXS and WAXS. Highly brilliant synchrotron X-ray allows high resolution study on weak, possibly diffuse scattering. We determined that the peak is off the equator and tilted from the virtical q_z axis.

4.2   Materials and Methods

High resolution was achieved by the use of Germanium monochromator, 0.01% energy dispersion. Low resolution data were taken with multilayer monochromator with 1% energy dispersion.

To achieve small mosaic spread, samples were annealed at 60 ℃for at least 6 hours right before the experiment. Silicon wafers were cleaned just before use. 2:1 methanol: chloroform was used to dissolve DMPC. Sample were rocked continuously during solvent evaporation and dried further inside a glove box. Samples were then dried under a hood for 24 hours and in a vaccume chamber for 2 hours. Samples were stored in a refrigerator.

A thin piece of molybdenum was used to attenuate the beam. The attenuation length μ of X-ray in Mo is 6.433 μm for 8 keV and 13.74 μm for 10.55 keV [8]. For a nominal 25 μm thick Mo attenuator, $\mu = 13.74$ gives the attenuation factor of $[\exp(-25/13.74)]^{-1} = 6.2$. The exact attenuation factor was determined by taking images with and without the attenuator and calculating a factor that needed to be multiplied for the images to match with each other.

Low angle scattering was done with low resolution setup.

25 μm silicon wafer was used to deposite our sample. This wafer absorbs only 20% of the X-ray beam at 10.5 keV (Check this). This weak absorption allows transmission

scattering. Trasmission experiment was done with low resolution setup.

Near grazing incident wide angle X-ray scattering experiment was done with both high and low resolution setups. To minimize geometric broadening in grazing angle experiment, the sample was trimmed to either 1 or 2 mm.

4.2.1 Sample Preparation

DMPC was purchased from Avanti Polar Lipids and used without further purification. Oriented thin film was deposited following the rock and roll procedure. In previous synchtrotron experiments, the samples were created and annealed more than a week in advance and stored in a refrigerator. The orientation quality of these samples were found to be worse than the quality soon after the samples were annealed. Therefore, to ensure the best sample quality, the sample was annealed for approximately 12 hours just before the X-ray experiment. Figure X compares a sample scattering in 2011 and 2013 synchrotron runs. Because of substantial degree of mosaic spread in the 2011 sample, many peaks overlapped, rendering the accurate measurement of integrated intensity difficult. Figure XX shows a picture of the annealing chamber. To achieve gentle but efficient hydration of a sample, filter papers were installed to cover the sample. For successful annealing, it must be emphasized that the annealing chamber equilibrates in the over prior to putting the samples in the chamber. When the sample was put in the chamber with its water at room temperature and then the system was placed inside the oven, warm vapor condensed on the cooler sample, causing so called flooding of oriented sample. A small drop of water on the oriented film was deterimental for the orientation because the bilayers tend to peel off, resulting in entropy-driven formation of unoriented vesicles in the water subphase.

The sample for grazing incident wide angle study was prepared in the same way as for low angle study. In order to minimize the geometric broadening, the sample was further trimmed down to 1 mm in width.

The sample for transmission study was deposited on a thin, 35 micron, silicon wafer. Because the wafer was very fragile, attaching the sample to a sticky thing was impossible. Instead, the sample was attached to a plastic cap of a small vial with a small amount of heat sink compound at a conrner of the wafer. The wafer was stable enough for rocking. The sample deposited on a glass cover slip (70 microns) was prepared similarly.

4.2.2 Low Angle X-ray Scattering Experiment

The same setup as described in Tat chapter was used for low angle diffraction experiment. In order to achieve a D-spacing comparable to that of Wack and Webb ($D \approx 57.9$ Å), the current to the Peltier was reversed, which heats the Peltier surface the sample was situated on.

The integrated intensity of each peak was obtained by putting a box around a peak and summing up the intensity in those pixels that fall inside the box. The background scattering was estimated by measuring the intensity in pixels near the peak but not containing any peak tail. The choice of box side was made according to the width of each peak. Because of mosaic spread in the sameple, peaks were wider for higher orders. Accordingly, the box was made wider for higher orders. The box size was chosen so that approximately 90% of the peak intensity was counted toward the integrated intensity.

A few peaks in the ripple phase were very strong, leading to saturation of CCD pixels. A nominally 25 micron molybdinum attenuator was inserted in the upstream to reduce the intensity of the X-ray beam and one second exposure was collected. The integrated intensity of the most strong, (1,0) peak was measured from this short exposure. To measure the actual attenuation factor, a one second exposure without the attenuator was also taken. Comparison of these two images yielded an attenuation factor of 7.8. The intensity of (2,0) and (2,-1) peaks were also measured in this one second exposure with an attenuator. All the other peaks were observed without saturation in 60 second exposure. To properly scale the strong orders, (1,0) peak intensity was multipied by 7.8 x 60 and (2,0) and (2,-1) were multiplied by 60.

The integrated intensity, peak position in pixel, the size of box, and estimated background for all the peaks are shown in Appendix.

4.2.3 Near Grazing Incident Wide Angle X-ray Scattering Experiment

Instead of multilayer monochromator with 1% energy dispersion, silicon monochromator with $\Delta E/E$ of 0.001% was used to achieve a higher resolution than that for the low angle X-ray scattering experiment.

4.2.4 Transmission Wide Angle X-ray Scattering Experiment

The axis of rotation does not coincide with the plane of the sample, so that the sample-to-detector distance is not fixed for different motor angle. The sample-to-detector distance was estimated from the setup geometry. We used 35 μm thin Si wafer, which absorbs x-ray by only 10%.

4.3 Some Theories

4.3.1 Lattice Structure

It has been shown from X-ray studies (ref) that ripples in in different bilayers are registered to form a two-dimensional oblique lattice as shown by the unit cell in Fig. X. The unit cell vectors in the ripple phase can be expressed as

$$\mathbf{a} = \frac{D}{\tan\gamma}\hat{\mathbf{x}} + D\hat{\mathbf{z}} \tag{4.1}$$

and

$$\mathbf{b} = \lambda_r\hat{\mathbf{x}}. \tag{4.2}$$

The corresponding reciprocal lattice unit cell vectors are

$$\mathbf{A} = \frac{2\pi}{D}\hat{\mathbf{z}} \tag{4.3}$$

and

$$\mathbf{B} = \frac{2\pi}{\lambda_r}\hat{\mathbf{x}} - \frac{2\pi}{\lambda_r\tan\gamma}\hat{\mathbf{z}}. \tag{4.4}$$

The reciprocal lattice vector, $\mathbf{q}_{hk}$ for the Bragg peak with Miller indices (h,k) is

$$\mathbf{q}_{hk} = h\mathbf{A} + k\mathbf{B}, \tag{4.5}$$

48

so its Cartesian components are

$$q_k^x \equiv q_{hk}^x = \frac{2\pi k}{\lambda_r} \tag{4.6}$$

$$q_{hk}^y = 0 \tag{4.7}$$

$$q_{hk}^z = \frac{2\pi h}{D} - \frac{2\pi k}{\lambda_r \tan \gamma}. \tag{4.8}$$

4.3.2 Sample q-space

The incoming and outgoing wavevectors of the x-ray beam in Fig. XXX are given by

$$\mathbf{k}_{\text{in}} = \frac{2\pi}{\lambda} \hat{\mathbf{y}}, \quad \mathbf{k}_{\text{out}} = \frac{2\pi}{\lambda} \left(\sin 2\theta \cos \phi \, \hat{\mathbf{x}} + \cos 2\theta \, \hat{\mathbf{y}} + \sin 2\theta \sin \phi \, \hat{\mathbf{z}} \right), \tag{4.9}$$

where λ is the wavelength of x-ray, 2θ is the total scattering angle, and ϕ is the angle measured from the equator on the detector. The scattering vector (also called momentum transfer vector) is the difference between $\mathbf{k}_{\text{in}}$ and $\mathbf{k}_{\text{out}}$,

$$\mathbf{q} = \mathbf{k}_{\text{out}} - \mathbf{k}_{\text{in}}$$
$$= q \left(\cos \theta \cos \phi \, \hat{\mathbf{x}} - \sin \theta \, \hat{\mathbf{y}} + \cos \theta \sin \phi \, \hat{\mathbf{z}} \right), \tag{4.10}$$

where $q = 4\pi \sin \theta / \lambda$ is the magnitude of the scattering vector. When the sample is rotated by ω about the lab x-axis in the clockwise direction as shown in Fig. XXX, the sample q-space also rotates and are given by

$$\hat{\mathbf{e}}_{\mathbf{x}} = \hat{\mathbf{x}}, \quad \hat{\mathbf{e}}_{\mathbf{y}} = \cos \omega \, \hat{\mathbf{y}} + \sin \omega \, \hat{\mathbf{z}}, \quad \hat{\mathbf{e}}_{\mathbf{z}} = -\sin \omega \, \hat{\mathbf{y}} + \cos \omega \, \hat{\mathbf{z}}. \tag{4.11}$$

From Eq. (4.10) and (4.11), we find the sample q-space to be

$$q_x = \mathbf{q} \cdot \hat{\mathbf{e}}_{\mathbf{x}} = q \cos \theta \cos \phi,$$
$$q_y = \mathbf{q} \cdot \hat{\mathbf{e}}_{\mathbf{y}} = q \left(-\sin \theta \cos \omega + \cos \theta \sin \phi \sin \omega \right),$$
$$q_z = \mathbf{q} \cdot \hat{\mathbf{e}}_{\mathbf{z}} = q \left(\sin \theta \sin \omega + \cos \theta \sin \phi \cos \omega \right). \tag{4.12}$$

The position, (X, Z), of a CCD pixel is measured with respect to the beam and given by

$$X = S \tan 2\theta \cos \phi, \quad Z = S \tan 2\theta \sin \phi, \tag{4.13}$$

where S is the distance between the sample and detector. From a model for the electron density of a lipid bilayer, one calculates a X-ray scattering intensity pattern, $I(\mathbf{q})$. Then, Eq. (4.12) and (4.13) relate $I(\mathbf{q})$ to the experimentally measured intensity pattern, $I(X,Z)$. It is important to remember that a given pixel position, (X,Z), corresponds to a triplet (q_x, q_y, q_z). Fully exploring the sample q-space requires changing ω for a fixed wavelength, which was achieved by continuously rotating the sample with a motor. In the ripple phase, because our sample has in-plane rotational symmetry, the ripple side peaks make up Bragg rings while the main peaks are still delta function like (see Fig. X) in q-space. In order for the main peak to be observed, ω must be equal to θ_{B}, but the side peaks are observed at any ω. Those side peaks get slightly smeared due to integration over q_y.

For low angle x-ray scattering (LAXS), it is convenient to linearize the above equations in terms of θ and ω. In the small angle approximation, $\sin\phi \approx Z/(2S\theta)$ and $\cos\phi \approx X/(2S\theta)$, and

$$
\begin{aligned}
q_x &\approx \frac{4\pi\theta\cos\phi}{\lambda} \approx kX/S \\
q_y &\approx q_z\omega - \frac{4\pi\theta^2}{\lambda} \approx q_z\omega - \frac{\lambda q_z^2}{4\pi} \\
q_z &\approx \frac{4\pi\theta\sin\phi}{\lambda} \approx kZ/S,
\end{aligned}
\tag{4.14}
$$

with $k = 2\pi/\lambda$. For wide angle X-ray scattering, the exact relations given by Eq. (4.12) are necessary. Especially in the transmission experiment, where ω is large, an observed X-ray pattern appears nontrivial and becomes almost impossible to analyze without the use of Eq. (4.12).

4.3.3   Geometric (Lorentz) Correction

Our sample has in-plane rotational symmetry. This means that the sample consists of many domains with differing ripple directions, all domains being parallel to the substrate. In sample q-space, then, ripple side peaks become rings while main peaks are still points (see Fig. X). For an arbitrary incident angle, main peaks are not observed while side peaks are observed. In order to capture both main and side peaks in one X-ray exposure, the sample was continuously rotated. As a result of this rotation, main peaks become arcs that subtend an angle $2\theta_{h0}$, as shown in Fig. 4.1,

with its length equal to $2\theta_{h0}q_{h0}^z$. The detector records the cross sections of these arcs
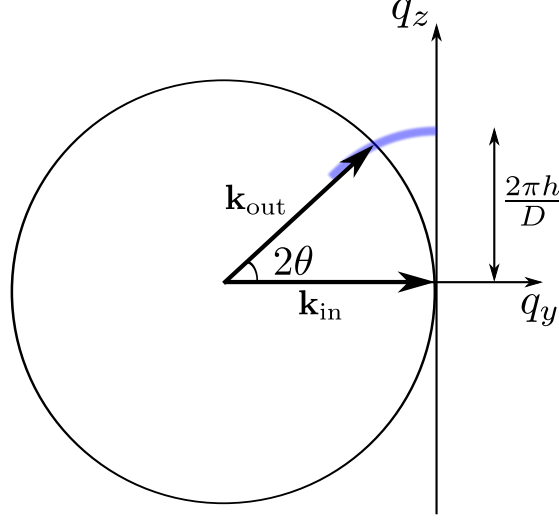
Figure 4.1: caption goes here

with the Ewald sphere, so the total scattering power is the product of the observed intensity, I_{hk}^{obs} with the arc length, that is,

$$I = 2\theta_{h0}q_{h0}^z I_{h0}^{\text{obs}}. \tag{4.15}$$

Because the sample has in-plane rotational symmetry, side peaks are represented as rings whose radius is q_{hk}^r. For a fixed incident angle, all the rings are intersected by the Ewald sphere. Because only the domains with the right ripple direction can satisfy the Bragg's condition at a given fixed angle, the scattering power of this small cross section is reduced by a factor of $2\pi q_k^r$ compared to main peaks. During an X-ray exposure, the rings cross the Ewald sphere at all incident angles. Then, the total scattering power is given by

$$I = 2\pi q_k^r I_k^{\text{obs}}. \tag{4.16}$$

Inverting Eq. (4.15) and (4.16) and realizing that the intensity is the form factor squared, we can calculate the observed intensity, I^{obs}, from a model for an electron density in the ripple phase.

Mathematically, the rotation is equivalent to an integration over ω. In low angle X-ray scattering, q_z is constant at a given pixel as ω is changed, which can be seen from Eq. (4.14). ω dependence appears only through q_y, so rotating the sample is realized by integrating over q_y. To derive the integration limits, let us consider two cases: (a)

51
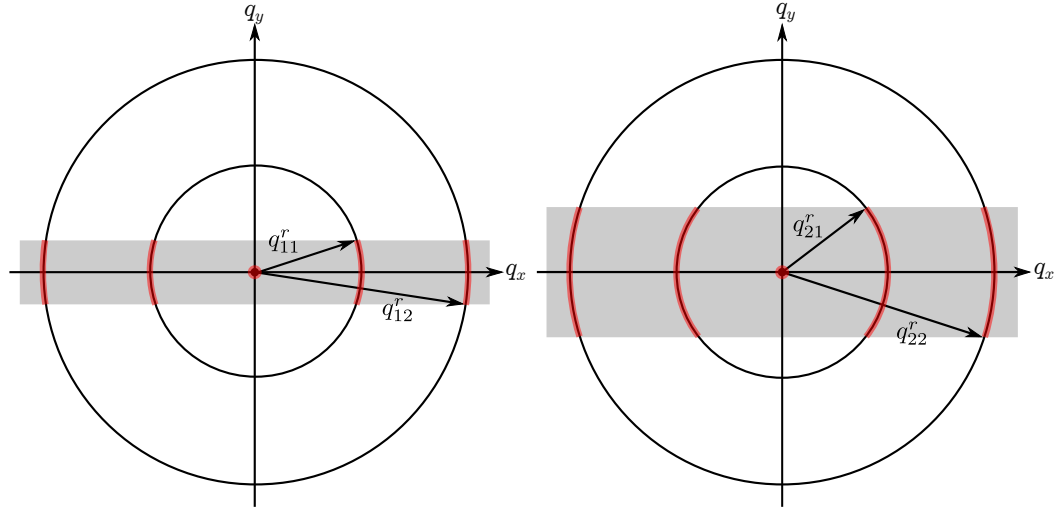
Figure 4.2: q-space representations of Bragg peaks and Bragg rings for $h = 1$ and k $= 0$, 1, and 2 in q_{hk}^z planes. The shaded rectangles show cross sections of the rotating Ewald sphere along q_{hk}^z plane. The intersection between the Ewald sphere and a Bragg peak/ring is indicated in red. The observed intensity for the $k \neq 0$ orders is proportional to the fraction of the length of red arcs in the circumference. This fraction is equal to one for a $k = 0$ order. Because the orders are not in the same q_z plane, the range of q_y integration indicated by the height of the rectangle is different for different orders. The magnitude of curvature of arcs is exaggerated.

When $\omega \leq 0$, the incoming X-ray beam is blocked by the back of the substrate. This sets the lower limit to 0. (b) When $\omega \geq 2\theta$, the substrate blocks the outgoing X-ray. Within the small angle approximation, then, $\omega_{\max}$ is $2 \times \lambda q_z/(4\pi)$ for scattering with q_z. Thus, the integration limits for q_y integration are $[-\lambda q_z^2/(4\pi), \lambda q_z^2/(4\pi)]$. We also need to integrate over X and Z to obtain integrated intensity. These lead to the observed intensity written as,

$$I_{hk}^{\text{obs}} \propto \int dX \int dZ \int d\omega |F_{hk}|^2 S_{hk}(\mathbf{q})$$

$$\propto |F_{hk}|^2 \int dq_x \int dq_z \int_{-\frac{\lambda q_z^2}{4\pi}}^{\frac{\lambda q_z^2}{4\pi}} \frac{dq_y}{q_z} S_{hk}(\mathbf{q}), \tag{4.17}$$

where $1/q_z$ factor in q_y integration is the Lorentz polarization factor in the small angle approximation.

For a crystalline sample with the in-plane rotational symmetry, the structure factor is

$$S_{hk}(\mathbf{q}) = S_{hk}(q_r, q_z) = \frac{1}{2\pi q_r} \delta(q_r - q_{r,k}) \delta(q_z - q_{z,hk}), \tag{4.18}$$

where $q_{r,k} = 2\pi |k|/\lambda_r$. Thus, the scattering pattern in the ripple phase is a collection of Bragg "rings" centered at the meridian and the Bragg peaks that are called the main peaks.

The observed, integrated intensity of hk peak is proportional to

$$I_{\text{o},hk} \propto \frac{|F_{hk}|^2}{q_{z,hk}} \int dq_x \int_{-q_{y0}}^{q_{y0}} dq_y \frac{\delta(q_r - q_{r,k})}{2\pi q_r}, \tag{4.19}$$

where $q_{y0} = \lambda q_{z,hk}^2/(4\pi)$. For side peaks ($k \neq 0$), we have

$$\int dq_x \int_{-q_{y0}}^{q_{y0}} dq_y \frac{\delta(q_r - q_{r,k})}{2\pi q_r} \approx \int_{-\frac{q_{y0}}{q_{r,k}}}^{\frac{q_{y0}}{q_{r,k}}} d\phi \int dq_r \, q_r \frac{\delta(q_r - q_{r,k})}{2\pi q_r}$$

$$= \frac{q_{y0}}{\pi q_{r,k}}. \tag{4.20}$$

For main peaks $(k = 0)$, we have

$$\int dq_x \int_{-q_{y0}}^{q_{y0}} dq_y \frac{\delta(q_r - q_{r,k})}{2\pi q_r} = \int_0^{2\pi} d\phi \int dq_r \, q_r \frac{\delta(q_r - q_{r,k})}{2\pi q_r}$$
$$= 1 \tag{4.21}$$

Using Eq. (4.20) and (4.21), we write the observed integrated intensity as

$$I_{\mathrm{o},h0} \propto \frac{|F_{h0}|^2}{q_{z,h0}} \tag{4.22}$$

$$I_{\mathrm{o},hk} \propto \frac{|F_{hk}|^2}{q_{z,hk}} \frac{q_{y0}}{\pi q_{r,k}} = |F_{hk}|^2 \frac{\lambda q_{z,hk}}{2\pi} \frac{1}{2\pi q_{r,k}} = |F_{hk}|^2 \frac{2\theta_{hk}}{2\pi q_{r,k}}, \tag{4.23}$$

where $2\theta_{hk} = \lambda q_{z,hk}/(2\pi)$ is the incident angle at which the outgoing X-ray for the peak (hk) is blocked by the substrate. Eq. (4.22) and (4.23) relate the form factor calculated from a model to the experimentally observed intensity, and are equivalent to Eq. (4.15) and (4.16), which were derived by using the Ewald sphere.

In nonlinear least-squares fitting procedure, we fitted the observed integrated intensity to the calculated intensity from a bilayer model using these geometrical corrections. This is because we can determine experimental uncertainties on observed intensity rather than the geometrically corrected form factors. We avoid propagating the uncertainties by fitting a model to observed intensity.

4.3.4 Absorption Correction for LAXS

In this section, we derive the absorption correction for the thin film sample. The calculation involves an explicit integration over the incident angle, ω, which is necessiated by the sample rotation during an x-ray exposure. The procedure is to write down an absorption factor, $A(\omega, \theta)$, for a given scattering angle at a given incident angle, and then integrate over ω. We ignore q_x dependence because the X-ray path inside the sample is nearly within the y-z plane for low angle scattering. The correction for wide angle scattering is described in a later section.

Assume that all the X-rays enter the sample from the top surface. The total scattering angle is given by 2θ (see Fig. 4.3). Let z-axis point downward. At the top surface (air-sample interface), $z = 0$. For X-rays that travel to z and then scatter,

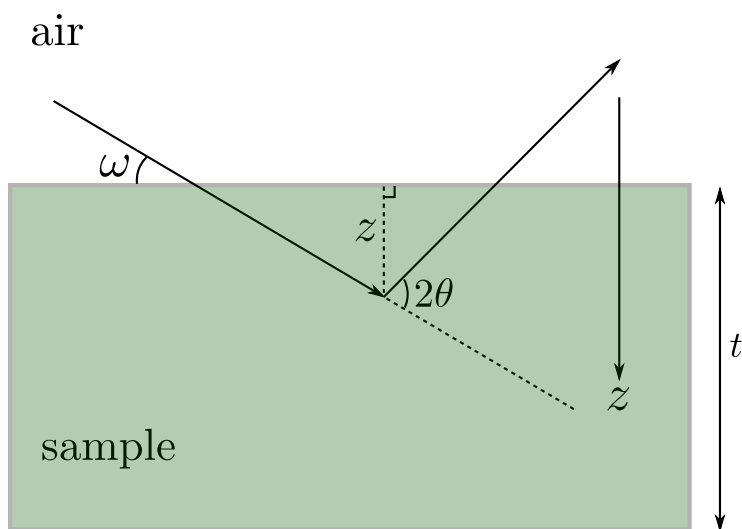Figure 4.3: The path of X-rays within the sample. The incident angle is ω and the total scattering angle is 2θ. An X-ray with a penetration depth of z is shown. The total thickness of the sample is t.

the total path length within the sample is

$$L_{\text{tot}}(z, \omega, \theta) = \frac{z}{\sin \omega} + \frac{z}{\sin(2\theta - \omega)} = zg(\omega, \theta), \tag{4.24}$$

where $g(\omega, \theta) = (\sin \omega)^{-1} + (\sin(2\theta - \omega))^{-1}$. For each ray, the intensity is attenuated by the sample absorption. If non-attenuated intensity is equal to I_0, then the attenuated intensity is

$$I(z, \omega, \theta) = I_0 \exp\left(-\frac{L_{\text{tot}}}{\mu}\right), \tag{4.25}$$

where μ is the absorption length of an X-ray. μ is 111 for 10.5 keV and 222 for 8 keV [8]. The observed intensity of scattering from a sample fixed at an angle ω is equal to the integration of Eq. (4.25) over the whole sample and given by

$$
\begin{aligned}
I_{\text{obs}}(\omega, \theta) &= \int_0^t dz\, I(z, \omega, \theta) = I_0 \int_0^t dz \exp\left(-\frac{g(\omega, \theta)}{\mu} z\right) \\
&= I_0 \mu \frac{1 - \exp\left(-\frac{t}{\mu} g(\omega, \theta)\right)}{g(\omega, \theta)}.
\end{aligned} \tag{4.26}
$$

Defining the absorption factor at a fixed angle to be $A(\omega, \theta)$, the observed intensity can be written as

$$I_{\text{obs}}(\omega, \theta) = A(\omega, \theta) t I_0, \tag{4.27}$$

where $t I_0$ is the intensity we would observe for non-absorbed X-rays. Equating Eq. (4.26) and (4.27), we get

$$A(\omega, \theta) = \frac{\mu}{t} \frac{1 - \exp\left(-\frac{t}{\mu} g(\omega, \theta)\right)}{g(\omega, \theta)}. \tag{4.28}$$

The total observed intensity from a sample that is being rotated during an exposure is simply

$$I_{\text{total}}(\theta) = \int_0^{2\theta} d\omega\, I_{\text{obs}}(\omega, \theta). \tag{4.29}$$

The upper integration limit is equal to 2θ because the substrate completely blocks the scattered X-rays above this angle as discussed in section 4.3.3.

Because the total non-attenuated intensity is given by $t\omega I_0$,

so that the total absorption factor is equal to

$$A(\theta) = \frac{\mu}{2\theta t} \int_0^{2\theta} d\omega \frac{1 - \exp\left(-\frac{t}{\mu}g(\omega)\right)}{g(\omega)}. \tag{4.30}$$

If μ is taken to infinity (no absorption), A goes to 1 as expected. Here, it is important to note that $1/2\theta$ factor in the above equation is normally called Lorentz polarization factor, which is usually approximated as $1/q_z$ for LAXS analysis. Since the SDP program applies this correction factor in addition to the absorption correction, we remove this factor in the formula for A_c. Therefore, the final result for the total absorption correction is

$$A_c(\theta) = \frac{1}{2\theta A(\theta)} = \frac{t}{\mu} \left[\int_0^{2\theta} d\omega \frac{1 - \exp\left(-\frac{t}{\mu}g(\omega)\right)}{g(\omega)} \right]^{-1}$$

with $g(\omega) = 1/\sin\omega + 1/\sin(2\theta - \omega)$.

4.3.5 Absorption Correction for WAXS

4.4 Model

4.4.1 Contour Part of the Form Factor

As in ref, we take the ripple profile to have a sawtooth-like profile. Its amplitude is $A/2$ and the projection of the major arm on the ripple direction is x_0 as shown in Fig. X. Then, we write the ripple profile as

$$u(x) = \begin{cases} -\frac{A}{\lambda_r - x_0}\left(x + \frac{\lambda_r}{2}\right) & \text{for} & -\frac{\lambda_r}{2} \leq x < -\frac{x_0}{2}, \\ \frac{A}{x_0}x & \text{for} & -\frac{x_0}{2} \leq x \leq \frac{x_0}{2}, \\ -\frac{A}{\lambda_r - x_0}\left(x - \frac{\lambda_r}{2}\right) & \text{for} & \frac{x_0}{2} < x \leq \frac{\lambda_r}{2}. \end{cases} \tag{4.31}$$

The ripple profile has the inversion symmetry, so that the resulting form factor is real. A and x_0 are fitting parameters that depend on the integrated intensity of each peak while D and λ_r are determined from measuring the positions of the Bragg peaks.

In order to allow the electron density along the ripple direction to modulate, we include two additional parameters, one to allow for the electron density across the

minor side to be different by a ratio f_1 from the electron density across the major side and a second parameter f_2, which is multiplied by δ functions $\delta(x \pm x_0/2)$ to allow for a different electron density near the kink between the major and the minor sides.

4.4.2   Transbilayer Part of the Form Factor

SDF

Delta function model is described here.

2G model

In the hybrid model, the terminal methyl region of the bilayer is represented as a Gaussian function [9]. The headgroups are represented by one and two Gaussian functions in 1G and 2G hybrid model, respectively. The methylene and water regions are each treated as a constant. The gap between the two constants is represented by a sine function. Then, for half of the bilayer, $0 \leq z \leq D/2$, the electron density has the form,

$$\rho(z) = \rho_{\mathrm{G}}(z) + \rho_{\mathrm{S}}(z) + \rho_{\mathrm{B}}(z), \tag{4.32}$$

where the Gaussian part is given by

$$\rho_{\mathrm{G}}(z) = \sum_{i=1}^{1 \text{ or } 2} \rho_{\mathrm{H}i} e^{-(z-Z_{\mathrm{H}i})^2/(2\sigma_{\mathrm{H}i}^2)} + \rho_{\mathrm{M}} e^{-z^2/(2\sigma_{\mathrm{M}}^2)}, \tag{4.33}$$

the strip part is given by

$$\rho_{\mathrm{S}}(z) = \begin{cases} \rho_{\mathrm{CH}_2} & \text{for} \quad 0 \leq z < Z_{\mathrm{CH}_2}, \\ \rho_{\mathrm{W}} & \text{for} \quad Z_{\mathrm{W}} \leq z \leq D/2, \end{cases} \tag{4.34}$$

and the bridging part is given by

$$\rho_{\mathrm{B}}(z) = \frac{\rho_{\mathrm{W}} - \rho_{\mathrm{CH}_2}}{2} \cos\left[\frac{-\pi}{\Delta Z_{\mathrm{H}}}(z - Z_{\mathrm{W}})\right] + \frac{\rho_{\mathrm{W}} + \rho_{\mathrm{CH}_2}}{2} \quad \text{for} \quad Z_{\mathrm{CH}_2} < z < Z_{\mathrm{W}}. \tag{4.35}$$

with $\Delta Z_{\mathrm{H}} = Z_{\mathrm{W}} - Z_{\mathrm{CH}_2}$. Here, we assume $Z_{\mathrm{H}2} > Z_{\mathrm{H}1}$. Table 4.1 shows some of the definitions. The transbilayer profile along $x = -z \tan \psi$ can be obtained by rotating the coordinates x and z by ψ in the clockwise direction and reexpressing $\rho(z)$ in terms

	1G	2G
Z_{CH_2}	$Z_{H1} - \sigma_{H1}$	$Z_{H1} - \sigma_{H1}$
Z_W	$Z_{H1} + \sigma_{H1}$	$Z_{H2} + \sigma_{H2}$

Table 4.1: Definitions of Z_{CH_2} and Z_W

of the rotated coordinates. This leads to replaincg x with $x' = x\cos\psi + z\sin\psi$ and z with $z' = -x\sin\psi + z\cos\psi$. Then, the rotated transbilayer profile is

$$\rho(x, z) = \delta(x + z\tan\psi)[\rho_G(z') + \rho_S(z') + \rho_B(z')]. \tag{4.36}$$

Taking the two dimensional Fourier transform of Eq. (4.36) leads to the transbilayer part of the form factor,

$$F_T = \int_{-\frac{D}{2}}^{\frac{D}{2}} \int_{-\frac{\lambda_r}{2}}^{\frac{\lambda_r}{2}} [\rho(x, z) - \rho_W]e^{i(q_x x + q_z z)} dx dz \tag{4.37}$$

$$= F_G + F_S + F_B. \tag{4.38}$$

The form factor is calculated in the minus fluid convention, where the bilayer electron density is measured with respect to the electron density of the surrounding solvent. The expression for F_T is rather messy and not shown. The derivation and full expression can be found in the appendix. Here, we note that the fitting parameters in this model are Z_{Hi}, σ_{Hi}, and R_{HiM} for each of the two headgroup Gaussian functions, σ_M for the terminal methyl Gaussian, ΔR for the methylene region, ψ for the lipid tilt, and an overall scaling factor. The contour part of the form factor has four more parameters (A, x_0, f_1, and f_2). In total, the modified 2G hybrid model implements 14 structural parameters.

4.5   Results

4.5.1   Data

Table 4.2 summarizes data we analyzed. As shown, we measured scattering in a almost identical conditions as the Wack and Webb's. This data allowed us to check our data obtained by using an oriented sample against an unoriented sample. As discussed earlier, these two types of samples give different Lorentz correction. We derived the

	λ_r	D	γ
WW	141.7	57.94	98.4°
S1	145	57.8	98.2°
S2	?	?	?

Table 4.2: Lattice constants

Lorentz correction for our oriented sample. Applying the derived correction to our data and calculating the form factor, we were able to confirm our correction. This check is shown in Table.

Figure shows a LAXS pattern from DMPC at 18 °C. $D = 57.9$ Å. Low resolution experiment. Up to $h = 9$ orders were observed in this data set. Because of a non-negligible degree of mosaicity in the sample, strong orders cast their arcs over weaker orders. A care must be taken to decompose the intensity at a given pixel to intensity due to a strong order's arc and to that due to a weak peak. This was achieved by taking a q_z swath and fitting the intensity to two Gaussian functions whose widths were determined from the known instrumental resolution. Figure shows an example of this operation. Table and Table show with and without the decomposition operation, respectively. For many of the orders observed, errors one would expect from neglecting the mosaicity effect were small. For higher orders, however, this was crucial to obtain the correct integrated intensity.

In order to test the decomposition effect, fits were also performed for the sum of intensity for orders that overlap.

First, we fitted the data using only up to $h = 3$ orders. What did we get? How did each model do? Any inconsistency witht Sun PNAS?

Next, we fitted every peak we observed. Which model failed?

4.5.2   Electron Density Profile

Table X shows the best fit for each model. It shows that the delta function model fails. Its failure is obviously due to its lack of fine structural details. In ref. (SUN), the model marginally worked because only up to the third orders were available. With the high flux synchrotron X-ray beam, many more higher orders were observed, whose intensity is dominated by finer details in the bilayer electron density. The table shows that 1G model also fails. 2G model works, but simple 2G model failed. $k = 6$ orders clearly require the modulation in the electron density along the ripple direction. The

phase of lower orders tends to be the same throughout the different models while higher orders vary widely. These are just ideas. I need to do actual fitting.

4.5.3 Near Grazing Incident Wide Angle X-ray Scattering (NGIWAXS)

Convert the image to q-space. Show the two resolved peaks. Measure the positions of these peaks. Can we confirm that the observed weak diffuse scattering is not the mosaic spread, but true sample scattering? Comment on the widths of the peaks observed. Possibly make use of both low and high resolution data. Apply the absorption correction.

4.5.4 Transmission WAXS

Convert the image to q-space. No strong order on the equator. Subtraction of water scattering from the background image. Compare to NGIWAXS and comment on the absorption effect in NGIWAXS data.

4.6 Discussion

Comparison with previous unoriented/oriented stuff?

Which theories are consistent/inconsistent with the results of this study?

4.7 Conclusion

Well, the ripple phase is the greatest phase in the lipid bilayers. Our detailed work lead to deeper insight into the formation of this phase. Future experiments include the high resolution transmission experiment, where both geometric broadening and energy dispersion are minimized. The expected resolution is the width of the X-ray beam, which is about 3 pixels. This experiment doubles the best resolution achieved in this work. Another slightly different high resolution experiment is to use silicon crystal analyzer downstread of the sample, which completely remove geoemtric boradening. The downside of this type of high resolution experiment is that only one

point in q-space is probed at any given exposure, so to get a full 2D map of wide angle scattering is time consuming.

Appendices

Bibliography

[1] Norbert Kuerka, John F. Nagle, Jonathan N. Sachs, Scott E. Feller, Jeremy Pencer, Andrew Jackson, and John Katsaras. Lipid bilayer structure determined by the simultaneous analysis of neutron and x-ray scattering data. *Biophysical Journal*, 95(5):2356 – 2367, 2008.

[2] Stephanie Tristram-Nagle, Yufeng Liu, Justin Legleiter, and John F. Nagle. Structure of gel phase DMPC determined by x-ray diffraction. *Biophysical Journal*, 83(6):3324 – 3335, 2002.

[3] Anthony R. Braun, Jonathan N. Sachs, and John F. Nagle. Comparing simulations of lipid bilayers to scattering data: The gromos 43a1-s3 force field. *The Journal of Physical Chemistry B*, 117(17):5065–5072, 2013.

[4] Berk Hess, Carsten Kutzner, David van der Spoel, and Erik Lindahl. Gromacs 4: Algorithms for highly efficient, load-balanced, and scalable molecular simulation. *Journal of Chemical Theory and Computation*, 4(3):435–447, 2008.

[5] Joakim P. M. Jmbeck and Alexander P. Lyubartsev. Derivation and systematic validation of a refined all-atom force field for phosphatidylcholine lipids. *The Journal of Physical Chemistry B*, 116(10):3164–3179, 2012.

[6] Joakim P. M. Jmbeck and Alexander P. Lyubartsev. An extension and further validation of an all-atomistic force field for biological membranes. *Journal of Chemical Theory and Computation*, 8(8):2938–2948, 2012.

[7] Viktor Hornak, Robert Abel, Asim Okur, Bentley Strockbine, Adrian Roitberg, and Carlos Simmerling. Comparison of multiple amber force fields and development of improved protein backbone parameters. *Proteins: Structure, Function, and Bioinformatics*, 65(3):712–725, 2006.

[8] `http://henke.lbl.gov/optical_constants`.

[9] M.C. Wiener, R.M. Suter, and J.F. Nagle. Structure of the fully hydrated gel phase of dipalmitoylphosphatidylcholine. *Biophysical Journal*, 55(2):315 – 325, 1989.